IRAS 16293-2422: Evidence for Infall onto a Counter-Rotating Protostellar Accretion Disk

Anthony J. Remijan[1,2] and J. M. Hollis[1]

ABSTRACT

We report high spatial resolution VLA observations of the low-mass star-forming region IRAS 16293-2422 using four molecular probes: ethyl cyanide (CH_3CH_2CN), methyl formate (CH_3OCHO), formic acid (HCOOH), and the ground vibrational state of silicon monoxide (SiO). Ethyl cyanide emission has a spatial scale of $\sim 20''$ and encompasses binary cores A and B as determined by continuum emission peaks. Surrounded by formic acid emission, methyl formate emission has a spatial scale of $\sim 6''$and is confined to core B. SiO emission shows two velocity components with spatial scales less than $2''$ that map $\sim 2''$ northeast of the A and B symmetry axis. The redshifted SiO is $\sim 2''$ northwest of blueshifted SiO along a position angle of $\sim 135^o$ which is approximately parallel to the A and B symmetry axis. We interpret the spatial position offset in red and blueshifted SiO emission as due to rotation of a protostellar accretion disk and we derive ~ 1.4 $M_\odot$ interior to the SiO emission. In the same vicinity, Mundy et al. (1986) also concluded rotation of a nearly edge-on disk from OVRO observations of much stronger and ubiquitous ^{13}CO emission but the direction of rotation is opposite to the SiO emission findings. Taken together, SiO and ^{13}CO data suggest evidence for a counter-rotating disk. Moreover, archival BIMA array ^{12}CO data show an inverse P Cygni profile with the strongest absorption in close proximity to the SiO emission, indicating unambiguous material infall toward the counter-rotating protostellar disk at a new source location within the IRAS 16293-2422 complex. The details of these observations and our interpretations are discussed.

Subject headings: ISM: abundances - ISM: clouds - ISM: individual (IRAS 16293-2422) - ISM: molecules - radio lines: ISM

---

[1]NASA Goddard Space Flight Center, Computational and Information Sciences and Technology Office, Code 606, Greenbelt, MD 20771

[2]National Research Council Resident Research Associate

1. INTRODUCTION

IRAS 16293-2422 is a low-mass star forming region located in the ρ Ophiuchus cloud complex at a heliocentric distance of 160 pc. It contains an undetermined number of protostellar objects, high velocity outflows in the E-W and NE-SW directions (Stark et al. 2004), and the region is dominated by two radio continuum peaks designated cores A and B. These two principal cores are separated by $\sim 5''$ and are often referred to as the "binary" system with a mass of 0.49 $M_\odot$ for core A and 0.61 $M_\odot$ for core B (Looney, Mundy & Welch 2000). Moreover, the gas and dust toward core A appears to be at a higher temperature than core B and most of the molecular emission lines of high energy transitions have been detected exclusively toward core A. The measured dust temperature toward core B is $\sim$40 K (Mundy et al. 1986) and the measured temperature toward core A from many different molecular species is between 80 and 200 K (Chandler et al. 2005).

Spectral observations with the IRAM 30-m radio telescope toward the low-mass protostellar system IRAS 16293-2422 (Cazaux et al. 2003) demonstrated an extremely rich organic inventory with abundant amounts of complex oxygen and nitrogen bearing molecules including formic acid (HCOOH), methyl formate (CH_3OCHO), acetic acid (CH_3COOH) and methyl cyanide (CH_3CN) which are archetypal species often found in massive hot molecular cores (HMCs). Subsequent spatial observations by Kuan et al. (2004) with the Submillimeter Array (SMA) mapped emission from high energy transitions of CH_3OCHO, vibrationally excited vinyl cyanide (CH_2CHCN) and other large molecular species. Additionally, Bottinelli et al. (2004) mapped slightly lower energy transitions of CH_3CN and CH_3OCHO with the Plateau de Bure interferometer, noting that all the molecular emission is contained toward cores A and B and that no large molecule emission is seen associated with the molecular outflows. Recently, Chandler et al. (2005) detected large abundances of a number of different organic molecular species primarily located toward core A from SMA observations. Moreover, from observations of sulfur monoxide (SO) absorbing against the background dust continuum near binary core B, Chandler et al. (2005) suggest that there must be material from an extended molecular envelope falling onto an embedded dust disk and that there may be a low-velocity outflow coming from an embedded protostar.

The discovery of large oxygen and nitrogen bearing molecules in a low-mass star forming region is significant because the molecular complexity appears to be similar to high-mass star forming regions. Such complex molecules undoubtedly are incorporated into subsequent formation of protoplanetary bodies and would provide a rich organic inventory that could be supplied to early planetary systems similar to that expected to have occurred in our own pre-solar nebula. With this in mind, we conducted high resolution observations of IRAS

16293-2422 using the NRAO[3] Very Large Array (VLA) using four molecular probes: ethyl cyanide (CH_3CH_2CN), methyl formate (CH_3OCHO), formic acid (HCOOH) and the ground vibrational state of silicon monoxide (SiO) to determine the implication of their relative spatial locations. Surprisingly, the location of SiO is not co-spatial with either core A or B. This prompted us to process archival BIMA array ^{12}CO data for an explanation.

2. OBSERVATIONS

Observations of IRAS 16293-2422 were conducted with the VLA in 2005 June 27 and 28 in its BnC configuration. Formic acid (HCOOH) and methyl formate (CH_3OCHO) were observed simultaneously in one correlator setting and ethyl cyanide (CH_3CH_2CN) and silicon monoxide (SiO) in another correlator setting. Table 1 lists the molecule (col. [1]), transition quantum numbers (col. [2]), rest frequency (col. [3]), upper energy level E_u (col. [4]), line strength S (col. [5]), dipole moment μ_a (col. [6]), and molecular parameter reference (col. [7]). The phase center for all observations was α= $16^h32^m22^s.8$, δ = -24°28′33″ (J2000.0). The correlator was operated in the four intermediate-frequency (IF) normal mode, and the selection of a 6.25 MHz bandpass yielded 32 spectral channels in two pairs of oppositely polarized IFs giving a channel width of 195.313 kHz (∼1.35 km s^{-1} at 44 GHz).

The compact radio source 1625-254 was used as the primary phase calibrator. The absolute flux density scale was determined from observations of 1331+305 (3c286) whose average flux density from the 2 observing bands was 1.44 Jy as given by the SETJY routine in AIPS. The averaged bootstrapped flux density of 1625-254 was 0.6 Jy. Antenna gains were derived from 1625-254 observations at 5 minute intervals. After ∼1 hr, a pointing calibration was performed to ensure pointing accuracy. All data were combined and calibrated using the AIPS data reduction package of NRAO. The calibrated $u - v$ datasets were then imported into MIRIAD (Sault et al. 1995) for imaging and deconvolution. Figures 1-4 show the images of the emission from CH_3CH_2CN, CH_3OCHO, HCOOH, and SiO, respectively toward IRAS 16293-2422.

The naturally weighted synthesized beamwidth resulting from the BnC configuration at 44 GHz was 0.″4×0.″3 and the largest angular size that can be measured in the BnC array is 43″. In order to determine the location and morphology of the molecular emission toward 16293-2422, the calibrated $u - v$ data were INVERTed using synthesized beams ranging from the naturally weighted synthesized beamwidth to a beamwidth of 20″×20″.

---

[3]The National Radio Astronomy Observatory is a facility of the National Science Foundation, operated under cooperative agreement by Associated Universities, Inc.

This process indicated whether the bulk of the emission from a given species was compact or extended and was utilized since: (1) emission from HCOOH, SiO ($J = 1 - 0$, v=0) and CH_3CH_2CN had not been previously mapped toward this region, and (2) no emission feature of low energy transitions (E_u<7.5 K) of large molecules had been imaged toward this region.

3. RESULTS AND DISCUSSION

3.1. CH_3CH_2CN

Figure 1 shows a contour map of the 5_{15}-4_{14} transition of CH_3CH_2CN superimposed on the 0.7 cm continuum emission (grayscale). The mapped CH_3CH_2CN emission region shows two blended emission peaks. Compared to the small naturally weighted beamwidth, a relatively large synthesized beamwidth of 10.″0×7.″5 is necessary to detect CH_3CH_2CN which is extended with respect to cores A and B and the oxygen bearing species (see § 3.2). Figure 1 also shows a hanning smoothed emission spectrum, which was extracted from the entire region of mapped emission, with an rms noise level of ∼7 mJy beam^{-1} shown on the left. The spectrum shows a relatively strong emission component at an LSR velocity of +7.7 km s^{-1} and a possible weaker component at +2.0 km s^{-1}. The systemic LSR velocity of +3.9 km s^{-1} (Bottinelli et al. 2004) is shown as a dashed line. We determine the total beam-averaged CH_3CH_2CN column density, N_T, using the formula:

$$N_T = 2.04 \frac{Q(T_{rot}) e^{(E_u/T_{rot})} \int \Delta I dv}{\theta_a \theta_b \nu^3 S_{ij}\mu^2} \times 10^{20} \mathrm{cm}^{-2}, \quad (1)$$

which is described in Remijan et al. (2004) where E_u is the upper state energy level (K); T_{rot} is the rotational temperature (K); θ_a and θ_b are the major and minor axes of the synthesized beam (arcsec); $\int \Delta I dv$ is the observed integrated line intensity (Jy beam^{-1} km s^{-1}); ν is the rest frequency (GHz); $S_{ij}\mu^2$ is the product of the transition line strength and the square of the electric dipole moment (Debye^2) and $Q(T_{rot})$ is the rotational partition function. N_T(EtCN) ∼ 5.2×10^{14} cm^{-2}, which assumes a rotational temperature of 54 K (Cazaux et al. 2003), is listed in Table 2. For a molecular hydrogen column density of 7.5×10^{22} cm^{-2} (Cazaux et al. 2003), the CH_3CH_2CN fractional abundance, X(EtCN), is 6.9×10^{-9}. These values are consistent to the column density of CH_3CH_2CN previously measured toward this source and is typical of the fractional abundance seen toward the Orion Compact Ridge (Cazaux et al. 2003).

The Figure 1 detection of extended emission with a spatial scale of ∼20" in a low-energy transition of CH_3CH_2CN demonstrates that there is a large envelope of cold molecular gas

surrounding the compact binary cores A and B. Core A is reputed to be hot (Chandler et al. 2005) while core B is thought to be much cooler (Mundy et al. 1986). A warm gas phase chemistry or grain surface chemistry can lead to enhanced emission from nitrogen bearing molecules in hot molecular cores (Remijan et al. 2004; Mehringer & Snyder 1996). In previous observations of IRAS 16293-2422 which sample high energy level transitions at 1 and 3 mm, enhanced emission of nitrogen bearing molecules have been detected toward cores A and B (e.g., CH_3CN by Bottinelli et al. 2004; HCN, HC_3N, and CH_2CHCN by Kuan et al. 2004) on a typical spatial scale of $\sim 5''$. Thus, our low-energy CH_3CH_2CN observations are complementary to these high-energy observations of other nitrogen bearing molecules, suggesting both increasing temperature and density gradients toward cores A and B.

3.2. CH_3OCHO and HCOOH

High energy transition of a number of different molecules have emission centroids near core A (e.g., see Figure 9 of Chandler et al. 2005); in particular, CH_3OCHO has high energy transitions that are associated with core A (Chandler et al. 2005; Bottinelli et al. 2004; Kuan et al. 2004). The only large oxygen bearing molecule detected by Chandler et al. (2005) toward core B is a low energy transition of dimethyl ether (CH_3OCH_3). Figures 2 and 3 show maps of low-energy transitions of CH_3OCHO and HCOOH, respectively, that are in proximity to core B. This is further evidence that core B is a much cooler protostellar core than core A. In Figure 2, the averaged emission from both the A and E states of CH_3OCHO are mapped using a synthesized beamwidth of $\sim 2.''6 \times 1.''8$. Figure 2 also shows an emission complex centered on the A and E states if one assumes an LSR velocity of $\sim +3.9$ km s^{-1}. This complex appears to be suffering from the competing effects of emission and self-absorption. In order to observe both states in the same bandpass, the average frequency (45.3966 GHz) of both states was used in the observations and this average frequency corresponds to an LSR velocity of +3.9 km s^{-1} in Figure 2 while the A and E states appear at -1.6 and +9.4 km s^{-1}, respectively. Figure 3 shows a map of the low-energy transition of HCOOH that surrounds the peak of core B and also the CH_3OCHO emission in Figure 2; no HCOOH emission was detected in the vicinity of core A. In Figure 3, the emission from HCOOH was mapped using a synthesized beamwidth of $\sim 2.''6 \times 1.''8$; similar to the beamwidth used to map the CH_4OCHO emission. The LSR velocity of HCOOH is $\sim +3.9$ km s^{-1} as indicated by the vertical dashed line in the spectrum also shown in Figure 3.

The spatial distributions of CH_3OCHO and HCOOH toward core B of IRAS 16293-2422 compare favorably to those same spatial distributions observed toward the Orion Molecular Cloud (OMC-1) compact ridge (Hollis et al. 2003; Liu et al. 2002). For example, in the OMC-

1 compact ridge, Hollis et al. (2003) observed HCOOH emission surrounding CH_3OCHO emission, and suggested that the HCOOH emission delineates the leading edge of a shock front as the outflow from source "I" interacts with the quiescent ambient gas; the CH_3OCHO emission, which is closer to source "I", then represents the post shock gas. If this scenario is correct for IRAS 16293-2422, then the corresponding outflow source associated with Figures 2 and 3 is likely core B itself. Indeed, Chandler et al. (2005) report evidence for material infall toward and also low-velocity outflow from core B; both conditions undoubtedly result in shock phenomena. Toward core A, enhanced abundances of large molecules provide indirect evidence for shocks to explain the enhancements (Chandler et al. 2005). The molecular differences between cores A and B are most likely explained by temperature differences and different protostellar ages. In any case, the presence of shocks seemingly leads to abundance enhancements in oxygen-bearing molecules, including large interstellar aldehydes located in high-mass star forming regions like Sgr B2 (e.g., see Hollis et al. 2004a, b).

Because the CH_3OCHO emission appears to be self-absorbed, we can only give a lower limit to the column density over the entire emission complex. Using 40 K for the rotational temperature (Mundy et al. 1986), N_T(MeF) $>1.9\times10^{16}$ cm^{-2}. Assuming an H_2 column density of 1.6×10^{24} cm^{-2} toward core B (Kuan et al. 2004), the CH_3OCHO fractional abundance is X(MeF) $>1.2\times10^{-8}$. For the same rotational temperature, N_T(HCOOH) $\sim 4.1\times10^{15}$ cm^{-2} and the HCOOH fractional abundance is X(HCOOH) $\sim 2.5\times10^{-9}$ (see Table 2).

3.3. SiO

Figure 4 shows redshifted and blueshifted SiO ($J = 1 - 0$, v=0), emission contours mapped separately over the 0.7 cm continuum (grayscale). These two components of the SiO emission are seen at LSR velocities of +2.3 km s^{-1} and +7.9 km s^{-1} which are approximately symmetrical around the systemic LSR velocity of 3.9 km s^{-1}. The peak intensity maps are shown at these velocities. The resulting synthesized beamwidth of $\sim$1.″5$\times$0.″8 is shown at the bottom left of the map. Also shown in Figure 4 is a spectrum which is averaged over the SiO emitting regions and hanning smoothed over 3 channels; the rms noise level is $\sim$3 mJy beam^{-1} shown to the left.

This is the first detection of the $J = 1 - 0$, v=0 transition of SiO toward IRAS 16293-2422 and the first map of the compact emission from SiO in the vicinity of cores A and B. Previous surveys by Blake et al. (1994) and Ceccarelli et al. (2000) detected weak emission features of higher energy transitions of v=0 SiO using single element radio telescopes. From a chemical model of the IRAS 16293-2422 region, Ceccarelli et al. (2000) concluded that an enhanced abundance of SiO was necessary to account for the excess emission from the

higher J level transitions and that the emission must be coming from a compact (<3″) region. Finally, their model calculated an infall velocity of SiO of 2.8 km s^{-1} which was consistent with their observed ∼5 km s^{-1} linewidths.

From our high resolution VLA observations, we find that the blue and redshifted SiO emission peaks have a spatial separation of ∼2″ and the center of the SiO emission centroid is located at α= $16^h32^m22^s.875$, δ = -24°28′32″.48 (J2000.0). This location is within 0.″6 of the pointing position and location of the ^{13}CO emission centroid taken with the Owens Valley Radio Observatory (OVRO) millimeter array (Mundy et al. 1986) and the peak position of CS emission taken with the IRAM 30-m (Menten et al. 1987). From the red and blueshifted emission peaks, Mundy et al. (1986) inferred a rotational velocity of 2 km s^{-1} and a rotating disk of material of 2 $M_\odot$ internal to the ^{13}CO emission. For the CS data, Menten et al. (1987) inferred a rotational velocity of 1.1 km s^{-1} from lower resolution observations a rotating disk of material of 4 $M_\odot$. From the high resolution SiO data, we determine a rotational velocity of ∼2.8 km s^{-1} and for a IRAS 16293-2422 distance of 160 pc, the mass interior to the SiO emission is ∼1.4$M_\odot$. However, assuming the SiO emission is associated with rotation, the compact disk containing the SiO emission is *counter-rotating* with respect to the previously reported ^{13}CO and CS emission. From archival BIMA array data taken of the $J = 2 - 1$ transition of ^{12}CO at 230.538 GHz, we find both emission and absorption toward IRAS 16293-2422. Moreover, the spectrum of the ^{12}CO data clearly show an inverse P Cygni profile with the strongest absorption in close proximity to the SiO emission (Figure 4), indicating unambiguously, material infalling toward the molecular disk. Chandler et al. (2005) also suggest there is evidence for infall toward core B from the absorption profile of SO taken with the SMA.

It is interesting to note that Schöier et al. (2005) have used the BIMA and OVRO arrays to observe a number of low energy transitions (i.e., the $J = 1 - 0$ of HCO^+, HNC, and N_2H^+ and the J = 2 - 1 of $C^{18}O$ and SiO) and also conclude, as we do, that these molecules indicate rotation about the direction perpendicular large-scale CO outflow in the NE-SW direction. This CO outflow has traditionally been associated with core source A. Compared to the VLA data presented in this work, these BIMA and OVRO data have an order of magnitude coarser spatial resolution that precludes an exact determination of the emission location which the VLA data have shown is ∼2″ north of core source A.

While it could be that the SiO complex we observe is due to outflow, evidence is accumulating to the contrary that rotation is the explanation. Such evidence is best seen on a small scale. For example, SiO observations in the present work show two velocity components each with linewidths of ∼5 km s^{-1}, suggesting rotation of a disk seen edge-on since the two components are not cospatial, are symmetric about an infall location, and have a velocity

gradient perpendicular to large-scale CO outflow. Moreover, images of other molecules on a small-scale also show that their velocity gradients are orthogonal to the direction of outflow seen on a large scale (e.g., Schöier et al. 2005). In this work, we have been very careful to match the synthesized beam to the source emission or absorption to pin-point the location of a new source of infall $\sim 2''$ north of core source A. We have done this by two independent sets of observations (i.e., the VLA in SiO emission and the BIMA array in ^{12}CO absorption). While there are no previous reports of continuum emission at this location, an inverse P Cygni profile is absolute proof of absorption against background continuum, and our BIMA data show that the location is smaller than the synthesized beam (i.e., $3.2'' \times 0.8''$). Thus, the continuum source is undoubtedly small (e.g. a disk seen edge-on) and may eventually be detected by an interferometer at high resolution with enough integration time.

In conclusion, we find a low temperature envelope of molecular CH_3CH_2CN emission that is encompassing the IRAS 16293-2422 cores A and B. Furthermore, low frequency, low energy transitions of large oxygen bearing molecules (i.e. HCOOH and CH_3OCHO) are seen toward core B where an outflow may be responsible for a low velocity shock that is leading to enhanced abundances of large oxygen bearing species. Finally, the SiO emission shows two velocity components with spatial scales less than $2''$ and a velocity separation of $\sim$5.6 km s^{-1}. We interpret the spatial position offset in red and blueshifted SiO emission as due to the rotation of a protostellar accretion disk and we derive ~ 1.4 M$_\odot$ interior to the SiO emission. However, the compact disk containing the SiO emission is *counter-rotating* with respect to the ^{13}CO and CS emission seen by other investigators. This is the first report of evidence for a counter-rotating accretion disk toward a low-mass protostellar complex. Moreover, archival BIMA array ^{12}CO data show an inverse P Cygni profile with the strongest absorption in close proximity to the SiO emission, indicating unambiguously, material infalling toward the counter-rotating protostellar disk. The infall location is compelling evidence for a new protostellar source within the IRAS 16293-2422 complex.

We thank C. Ceccarelli for valuable comments on this work, and R. Crutcher for permission to utilize the BIMA array data archive to explore ^{12}CO data toward IRAS 16293-2422. J.M.H. gratefully acknowledges research support from H.A. Thronson of the NASA Science Mission Directorate.

REFERENCES

Blake, G. A., van Dishoek, E. F., Jansen, D. J., Groesbeck, T. D., & Mundy, L. G. 1994, ApJ, 428, 680

Bottinelli, S., Ceccarelli, C., Neri, R., Williams, J. P., Caux, E., Cazaux, S., Lefloch, B., Maret, S., & Tielens, A. G. G. M. 2004, ApJ, 617, L69

Cazaux, S., Tielens, A. G. G. M., Ceccarelli, C., Castets, A., Wakelam, V., Caux, E., Parise, B., & Teyssier, D. 2003, ApJ, 593, L51

Ceccarelli, C., Castets, A., Caux, E., Hollenbach, D., Loinard, L., Molinari, S., & Tielens, A. G. G. M. 2000, A&A, 355, 1129

Chandler, C. J., Brogan, C. L., Shirley, Y. L., & Loinard L. 2005, ApJ, in press

Hollis, J. M., Jewell, P. R., Lovas, F. J., Remijan, A., Møllendal, H. 2004a, ApJ, 610, L21

Hollis, J. M., Jewell, P. R., Lovas, F. J., Remijan, A. 2004b, ApJ, 613, L45

Hollis, J. M., Pedelty, J. A., Snyder, L. E., Jewell, P. R., Lovas, F. J., Palmer, Patrick, & Liu, S.-Y. 2003, ApJ, 588, 353

Kuan, Y.-J., Huang, H.-C., Charnley, S. B., Hirano, N., Takakuwa, S., Wilner, D. J., Liu, S.-Y., Ohashi, N., Bourke, T. L., Qi, C., & Zhang, Q., 2004, ApJ, 616, L27

Liu, S.-Y., Girart, J. M., Remijan, A., Snyder, L. E. 2002, ApJ, 576, 255

Looney, L. W., Mundy, L. G., Welch, W. J. 2000, ApJ, 529, 477

Lovas, F. J. & Krupenie, P. 1974, J. Phys. Chem. Ref. Data, 3, 245

Lovas, F. J. 1982, J. Phys. Chem. Ref. Data, 11, 251

Mehringer, D. M., & Snyder, L. E. 1996, ApJ, 471, 897

Menten, K. M., Serabyn, E., Guesten, R., Wilson, T. L. 1987, A&A, 177, L57

Mundy, L. G., Myers, S. T., & Wilking, B. A. 1986, ApJ, 311, L75

Oesterling, L. C., Albert, S., de Lucia, F. C., Sastry, K. V. L. N., & Herbst, E. 1999, ApJ, 521, 255

Remijan, A., Shiao, Y.-S., Friedel, D. N., Meier, D. S., Snyder, L. E. 2004, ApJ, 617, 384

Sault, R. J., Teuben, P. J., & Wright, M. C. H. 1995, ASP Conf. Ser. 77: Astronomical Data Analysis Software and Systems IV, 77, 433

Schöier, F. L., Jørgensen, J. K., van Dishoeck, E. F., Blake, G. A., & Mundy, L. G. 2005, A&A, in preparation

Stark, R., Sandell, G., Beck, S. C., Hogerheijde, M. R., van Dishoeck, E. F., van der Wal, P., van der Tak, F. F. S., Schäfer, F., Melnick, G. J., Ashby, M. L. N., & de Lange, G. 2004, ApJ, 608, 341

Willemot, E., Dangoisse, D., Monnanteuil, N., & Bellet, J. 1980, J. Phys. Chem. Ref. Data, 9, 59

FIGURE CAPTIONS

Fig. 1.— Spectrum and map of the 5_{15}-4_{14} transition of CH_3CH_2CN. The spectrum, which was taken from the entire region of mapped emission, is hanning smoothed over 3 channels. The rms noise level of $\sim$7 mJy beam^{-1} is shown at the left. The systemic LSR velocity of +3.9 km s^{-1} is shown as a vertical dashed line. The contour map of the 5_{15}-4_{14} transition of CH_3CH_2CN is shown superimposed on 0.7 cm continuum emission (grayscale). The contour levels are -0.045, 0.045, 0.060, 0.075 and 0.09 Jy beam^{-1} (0.045 Jy beam^{-1} = 5 σ). The synthesized beamwidth is shown at the bottom left of the map.

Fig. 2.— Spectrum and map of the 5_{15}-4_{14} A and E state transitions of CH_3OCHO. The spectrum, which was taken from the entire region of mapped emission, is hanning smoothed over 3 channels. The rms noise level of $\sim$2 mJy beam^{-1} is shown at the left. The average frequency of the A and E state transitions appears at an LSR velocity of +3.9 km s^{-1}. The contour map of the CH_3OCHO emission is shown superimposed on 0.7 cm continuum emission (grayscale). The contour levels are -0.008, -0.010, 0.010, 0.012, 0.014 and 0.016 Jy beam^{-1} (0.010 Jy beam^{-1} = 5 σ). The synthesized beamwidth is shown at the bottom left of the map.

Fig. 3.— Spectrum and map of the 2_{02}-1_{01} transition of HCOOH. The spectrum, which was taken from the southernmost region of mapped emission toward core B, is hanning smoothed over 3 channels. The rms noise level of $\sim$2 mJy beam^{-1} is shown at the left. The spectrum shows the HCOOH emission is centered at the systemic LSR velocity of +3.9 km s^{-1} (vertical

dashed line). The contour map of the HCOOH emission is shown superimposed on 0.7 cm continuum emission (grayscale). The contour levels are -0.007, -0.009, 0.011, 0.014, 0.016 and 0.018 Jy beam^{-1} (0.011 Jy beam^{-1} = 5 σ). The synthesized beamwidth is shown at the bottom left of the map.

Fig. 4.— Spectrum and maps of the J=1-0, v=0 transition of SiO and spectrum of the J=2-1 transition of ^{12}CO at 230.538 GHz taken with the BIMA array. The spectrum of SiO was averaged over the emission regions and is hanning smoothed over 3 channels. The spectrum shows a redshifted and blueshifted components of SiO emission approximately centered at the systemic LSR velocity of +3.9 km s^{-1} (vertical dashed line). The 1 σ rms noise level of $\sim$2 mJy beam^{-1} is shown on the left. The contour map of the SiO emission is superimposed on the 0.7 cm continuum emission (grayscale) and shows the location of the redshifted and blueshifted emission peaks. The contour levels are -0.008, -0.010, 0.010, 0.011, 0.012, 0.013 and 0.014 Jy beam^{-1} (0.010 Jy beam^{-1} = 5 σ). The synthesized beamwidth of is shown at the bottom left of the map. Also shown in the map is the location of the emission trough of the inverse P Cygni profile of the ^{12}CO emission. The spectrum of the J=2-1 transition of ^{12}CO at 230.538 GHz has a 1 σ rms noise level of $\sim$1 Jy beam^{-1} (shown on the left of the spectrum). Additionally, the location of the maximum absorption of ^{12}CO is shown as a filled circle in proximity to the SiO emission in the maps.

Table 1. Molecular Line Parameters

Molecule (1)	Transition $J'_{K-,K+}$-$J''_{K-,K+}$ (2)	Frequency[a] (MHz) (3)	E_u (K) (4)	S (5)	μ_a (D) (6)	Reference (7)
SiO	1-0,v=0	43,423.864(22)	2.085	1.00	3.10	b
CH_3CH_2CN	5_{15}-4_{14}	43,516.200(8)	7.380	4.80	3.85	c
HCOOH	2_{02}-1_{01}	44,911.750(50)	3.238	2.00	1.39	d
CH_3OCHO	4_{14}-3_{13} E	45,395.755(16)	6.187	3.80	1.63	e
	4_{14}-3_{13} A	45,397.394(16)	6.187	3.80	1.63	e

[a]Uncertainties in parentheses refer to the least significant digit and are 2 σ values.

[b]Lovas & Krupenie 1974

[c]Lovas 1982

[d]Willemot et al. 1980

[e]Oesterling et al. 1999

Table 2. Molecular Column Densities

Molecule (1)	v_{LSR} Range (km s^{-1}) (2)	$\int$I dv (Jy bm^{-1} km s^{-1}) (3)	T_{rot} (K) (4)	N_T ($\times10^{14}$ cm^{-2}) (5)	X ($\times10^{-9}$) (6)
CH_3CH_2CN	+0.0 to +10.0	0.34(9)	54	5.2(1.4)	6.9(1.4)
CH_3OCHO	-5.0 to +16.0	>0.22	40	>187	>11.7
HCOOH	+0.0 to +8.0	0.07(3)	40	41(17)	2.5(1.7)

Note. — SiO is undoubtedly masering and is therefore not included in this table.

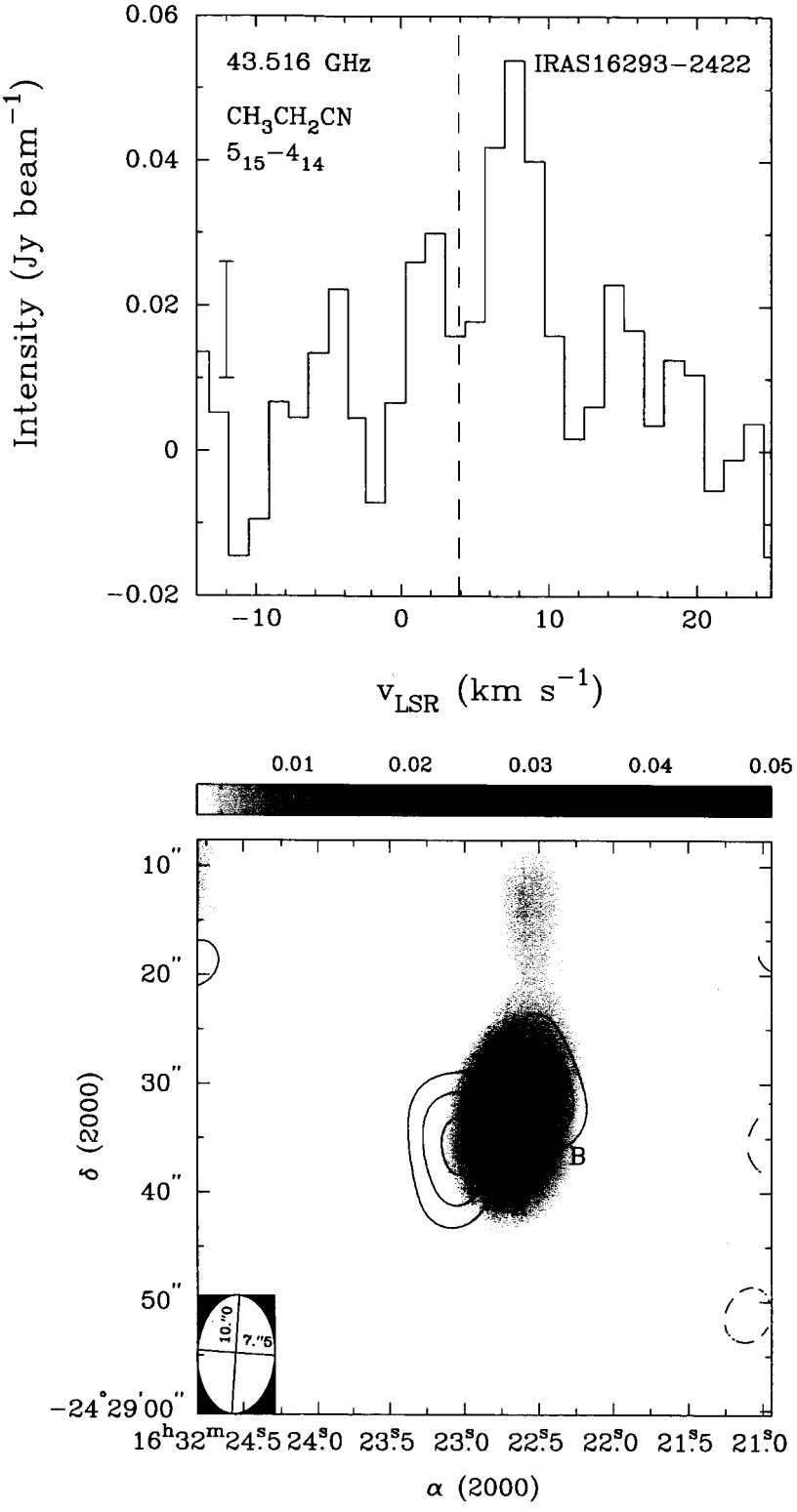
43.516 GHz
IRAS16293−2422
CH_3CH_2CN
$5_{15}-4_{14}$
Intensity (Jy beam^{-1})
0.06
0.04
0.02
0
−0.02
−10
0
10
20
v_{LSR} (km s^{-1})
0.01
0.02
0.03
0.04
0.05
B
10.″0
7.″5
δ (2000)
10″
20″
30″
40″
50″
−24°29′00″
16^{h}32^{m}24.^{s}5 24.^{s}0 23.^{s}5 23.^{s}0 22.^{s}5 22.^{s}0 21.^{s}5 21.^{s}0
α (2000)

Figure 1.

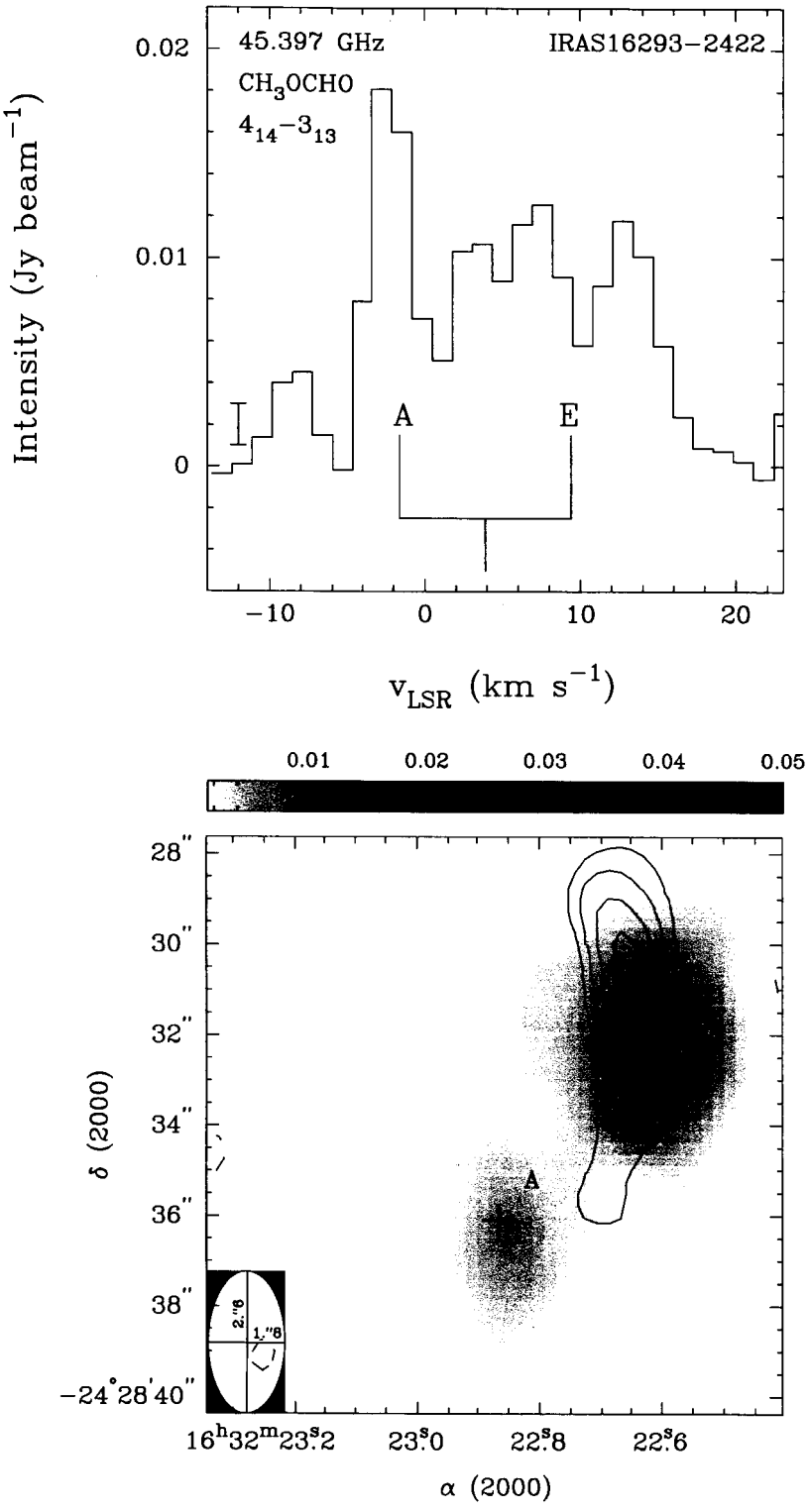
45.397 GHz
IRAS16293−2422
CH_3OCHO
$4_{14}-3_{13}$
A
E
Intensity (Jy beam^{-1})
0.02
0.01
0
−10
0
10
20
v_{LSR} (km s^{-1})
0.01
0.02
0.03
0.04
0.05
28″
30″
32″
34″
36″
38″
δ (2000)
−24°28′40″
2.″6
1.″8
A
16^{h}32^{m}23^s.2
23^s.0
22^s.8
22^s.6
α (2000)

Figure 2.

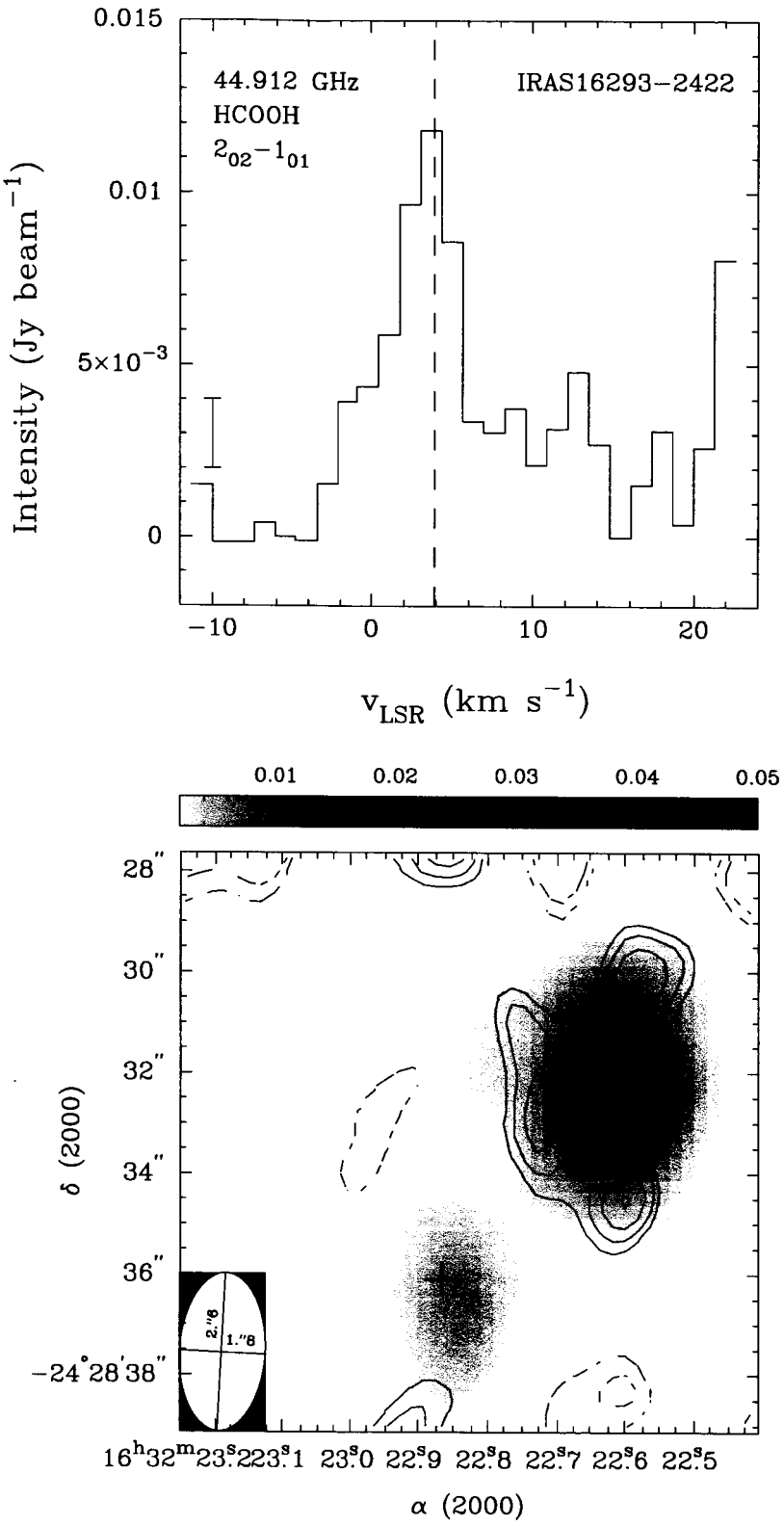
0.015
0.01
5×10^-3
0
44.912 GHz
HCOOH
2_02−1_01
IRAS16293−2422
Intensity (Jy beam^-1)
−10
0
10
20
v_LSR (km s^-1)
0.01
0.02
0.03
0.04
0.05
28″
30″
32″
34″
36″
δ (2000)
−24°28′38″
2.″6
1.″8
16^h32^m23^s.223^s.1
23^s.0
22^s.9
22^s.8
22^s.7
22^s.6
22^s.5
α (2000)

Figure 3.

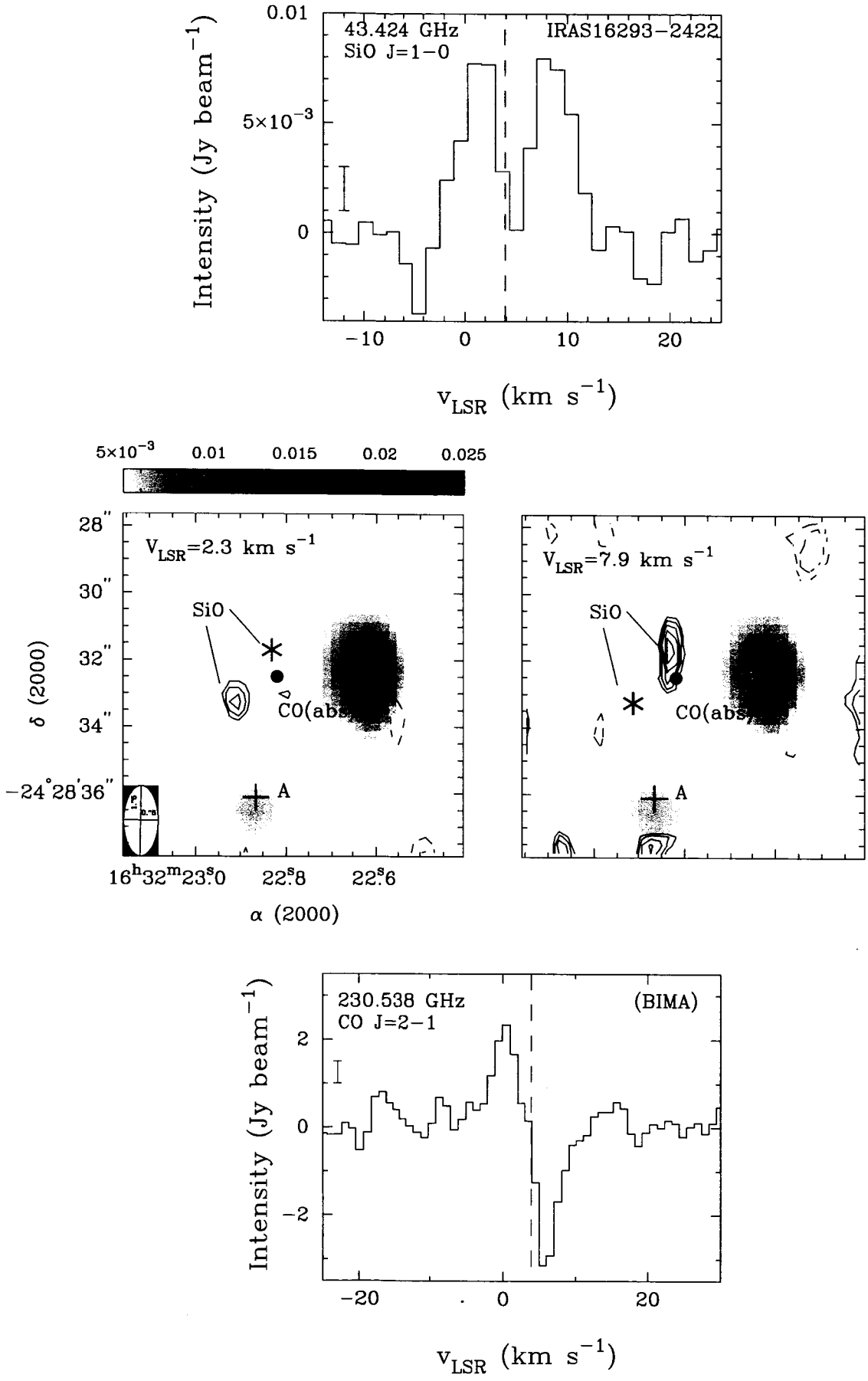
43.424 GHz
SiO J=1−0
IRAS16293−2422
Intensity (Jy beam^{-1})
0.01
5×10^{-3}
0
−10
0
10
20
v_{LSR} (km s^{-1})
5×10^{-3}
0.01
0.015
0.02
0.025
V_{LSR}=2.3 km s^{-1}
V_{LSR}=7.9 km s^{-1}
SiO
CO(abs)
A
28″
30″
32″
34″
δ (2000)
−24°28′36″
16^{h}32^{m}23^s.0
22^s.8
22^s.6
α (2000)
230.538 GHz
CO J=2−1
(BIMA)
Intensity (Jy beam^{-1})
2
0
−2
−20
0
20
v_{LSR} (km s^{-1})

Figure 4.